Reduction of degenerate four-wave mixing spectra to relative populations II. Strong-field limit

Skip Williams[a] and Richard N. Zare[b]
Department of Chemistry, Stanford University, Stanford, California 94305

Larry A. Rahn[b]
Combustion Research Facility (MS 9051), Sandia National Laboratories, Livermore, California 94551

The degenerate four-wave-mixing (DFWM) signal is said to be saturated when the population difference of the two levels involved in the resonant transition oscillates with a rate (Rabi frequency) greater than the relaxation and dephasing rates. The field intensity at which this occurs is referred to as the DFWM saturation intensity. We find that the DFWM saturation behavior predicted by nondegenerate two-level models is in close agreement with the observed power dependence of (0,0) band transitions of the CH A $^2\Delta - X$ $^2\Pi$ system. Furthermore, when the linear polarization states of the excitation fields are varied, the saturation intensity does not change significantly. In contrast, large differences in the DFWM signals are observed as a function of input field polarization and rotational branch. These differences are nearly independent of laser intensity. The DFWM signal differences are rationalized using the diagrammatic perturbation theory (DPT) expressions described in the preceding paper. We find that the DPT expressions are accurate to 10%–30% at saturating laser intensities. The important aspects of the reduction of saturated DFWM signals to relative internal-state distributions are outlined in environments where population relaxation and dephasing events are dominated by collisions, and a rotational temperature analysis is presented of the CH radical in an atmospheric-pressure oxyacetylene flame. Rotational temperatures determined using saturated DFWM are estimated to be accurate to 5%.

I. INTRODUCTION

Abrams and Lind (AL)[1] have presented a model of degenerate four-wave mixing (DFWM) which has shown good agreement with experiments.[2-4] The AL model considers a nondegenerate two-level homogeneously broadened system in the presence of two counterpropagating pump fields of arbitrary intensity and weak probe and signal fields. The probe and signal intensities are weak in the sense that they do not significantly affect the level populations. In this model all fields are monochromatic, are of the same polarization state, and are configured in the phase-conjugate geometry (PC-DFWM) discussed in the preceding paper (hereafter referred to as WZR1).[5]

One of the most significant predictions of the AL model is that the DFWM signal becomes relatively insensitive to collisions when the intensity of the pump fields is increased so that the population difference of the two-level system oscillates with a rate (Rabi frequency) greater than the relaxation and dephasing rates. When the pump field intensity approaches this value (I_{sat}^0) the DFWM signal is said to be saturated. The collisional independence of saturated DFWM has been verified experimentally for many species including NO,[6,7] OH,[8-10] NH,[11] and CH.[12] Note, however, that the AL model should be viewed only as a qualitative description of these experiments because in most cases the lasers employed are not monochromatic, the molecules are moving, and the probe field intensity is a significant fraction of the pump field

intensity. In addition, molecules possess polarization-dependent spectroscopic properties such as those discussed in WZR1 that are not described by the AL model.

Meacher, Charlton, Ewart, Cooper, and Alber (MCECA)[13-15] have developed a theory for DFWM with broad-bandwidth lasers that has shown qualitative agreement with experiments.[13] The MCECA model is similar to the AL model in that intense pump fields and a weak probe field interact with stationary nondegenerate two-level absorbers in a PC-DFWM phase matching geometry; however, the pump bandwidths are assumed to be much larger than the homogeneous line width (including power broadening) of the optical transition. In this model the probe bandwidth can be any size. The results show that increasing the pump bandwidth leads to an increased I_{sat}^0 and a slightly different DFWM power dependence compared to the AL model.

Lucht, Farrow, and Rakestraw (LFR)[16] have addressed the effects of molecular motion and strong (saturating) probe field intensity. LFR numerically evaluated the time- and space-dependent density matrix equations directly for a nondegenerate two-level system with molecular motion in which any or all of the incident fields can be saturating. LFR calculated DFWM intensities and line shapes for conditions of interest for flame and plasma diagnostics, and compared the results of their calculations to experimental results of NO in 100 Torr of helium excited by a narrow-bandwidth (0.004 cm^{-1}) laser. Some of the findings of LFR relevant to our work are as follows: first the presence of molecular motion slightly increases I_{sat}^0; second, when the probe field intensity is one quarter of the pump field intensity the DFWM saturation behavior is very similar to the case where the probe field
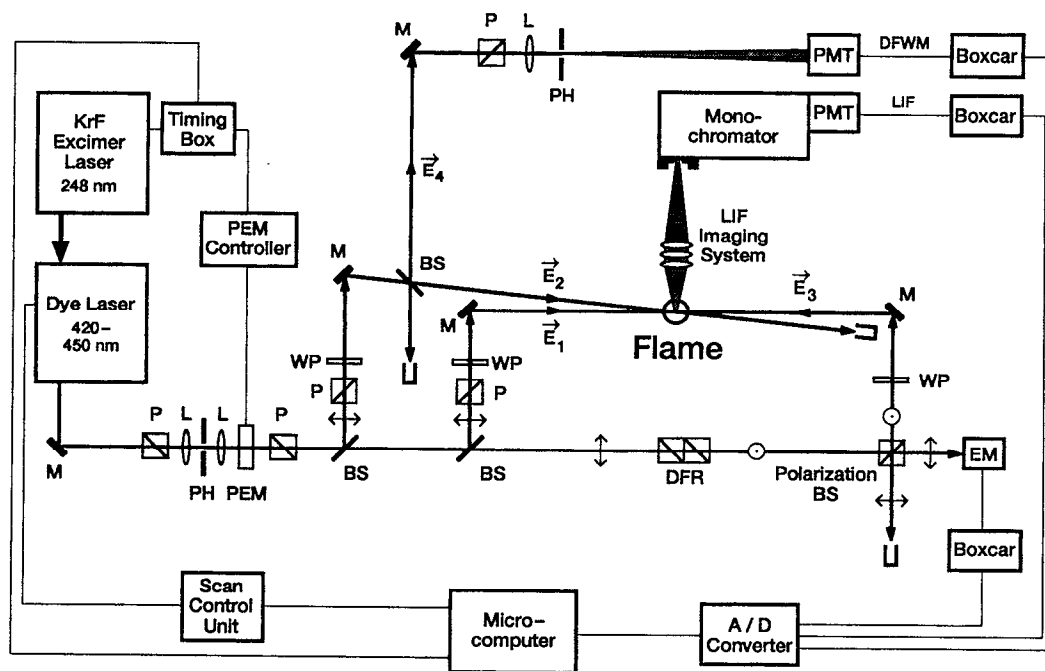

FIG. 1. Experimental configuration for the measurement of DFWM signals. Spectra are recorded with unfocused beams (diameter ~0.5 mm) having energies of 16 μJ for the pump beams (1 and 3) and 4 μJ for the probe beam (2). The flame consists of a standard welding torch fitted with a 0.94 mm nozzle. The abbreviations used in the figure are defined as follows: M: mirror, P: polarizer, L: lens, PH: pinhole, PEM: photoelastic modulator, BS: beamsplitter, WP: half-wave plate, DFR: double Fresnel rhomb, EM: energy meter, PMT: photomultiplier tube.

is held constant at a value much less than I_{sat}^0; and third, the DFWM signal is nearly independent of collisions when the pump field intensity is approximately $2I_{sat}^0$.

LFR discussed their work in the context of previous saturation treatments[17-24] so further comparisons will not be made here. The work of AL, MCECA, and LFR greatly enhance the understanding of DFWM saturation; however, because these models assume a nondegenerate two-level system, the effect of polarization in saturated DFWM remains unresolved.

Our aim is to determine the effect of polarization in applying nondegenerate two-level models to experiments involving molecules; in particular we wish to determine how polarization affects extracting relative internal-state distributions from DFWM signals. Our approach is to measure DFWM signals as a function field polarization and intensity and to interpret these data in the framework of the AL and MCECA models using the ideas developed in WZR1. In Sec. II we discuss the pertinent experimental details. A brief discussion of the AL and MCECA models is given in Sec. III with an emphasis on the key elements required to interpret DFWM signals. In Sec. IV we present DFWM data of the CH radical in an atmospheric-pressure flame as a function of field polarization and intensity, interpret the results, and present methods for extracting relative population distributions from saturated DFWM signals. In Sec. V we present conclusions of our findings.

II. EXPERIMENTAL DETAILS

A. Experimental apparatus

Figure 1 shows the experimental configuration in which three fields of the same frequency overlap in the reaction zone of an atmospheric-pressure oxyacetylene flame to generate a fourth field (the DFWM signal). The two coaxial and counterpropagating pump fields, denoted E_1 (forward pump) and E_3 (backward pump), are crossed at a small angle, $\theta = 2°$, by a probe field, E_2. This configuration is commonly referred to as the PC-DFWM geometry. The PC-DFWM signal field, E_4, is coherently generated and propagates 6 m to a photomultiplier (Hamamatsu R2393P) where it is detected.

Excitation is provided by a KrF excimer-pumped dye laser system (Lambda Physik EMG 102 MSC and FL 2002) operated over the wavelength range of 425–450 nm with a bandwidth of $\Delta\bar{\nu}_L = 0.18 \pm 0.02$ cm^{-1} (FWHM) and a pulse width of $\Delta\tau_L = 16.3 \pm 1$ ns (FWHM). The output beam of the dye laser is spatially filtered to produce a Gaussian beam profile. The FWHM diameter of the beams is measured using the procedure outlined in Ref. 25 and is typically $d_{fwhm} \sim 0.5$ mm. The beam diameter can be determined to ± 0.02 mm. The laser energy is computer (PC/XT) controlled using a photoelastic modulator (Hinds International PEM-CF4) between two crossed polarizers that allows the laser energy to be adjusted between 1 and 800 μJ with no beam deviation. The energy of the probe beam is one quarter of the forward pump beam, and the energy of the backward pump beam is
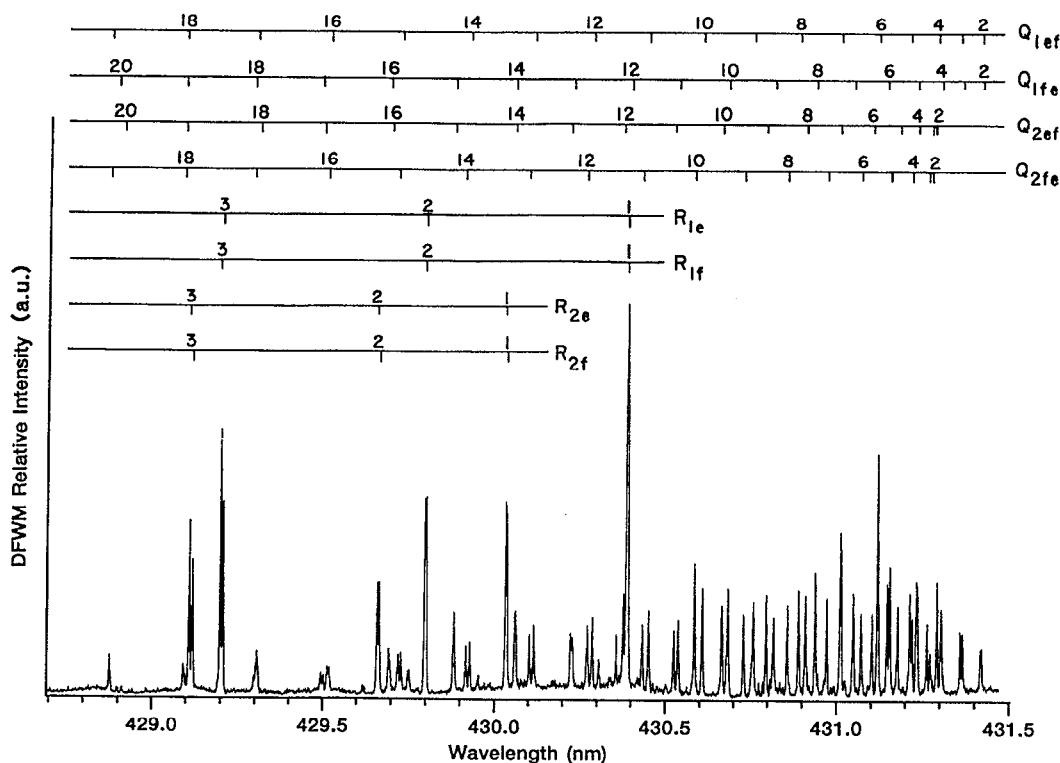
FIG. 2. DFWM spectrum of selected Q- and R-branch transitions of the CH A $^2\Delta - X$ $^2\Pi(0,0)$ and $(1,1)$ bands recorded using the $YYXX$ polarization configuration. In the figure only the $(0,0)$ band transitions are labeled. The fine-structure components are indicated on the branch designations by subscript $1 = {}^2\Delta_{5/2} - {}^2\Pi_{3/2}$ and subscript $2 = {}^2\Delta_{3/2} - {}^2\Pi_{1/2}$. The upper state and lower state Λ doublets are labeled by e and f; when they are the same for both levels, ee is abbreviated by e and ff is abreviated by f.

adjusted to the value of the forward pump beam using a double Fresnel rhomb and a polarization beamsplitter which reflects S-polarized and transmits P-polarized light. We measure the beam energy by placing an energy meter (Molectron J4-09) after the polarization beam splitter which allows the energy to be measured directly and accurately to a fraction of a microjoule.

The DFWM signal is amplified (Lecroy VV100BTB) before being processed by boxcar a averager (SRS SR250). The laser energy is processed directly by a boxcar averager (SRS SR250). Up to four channels are read at each wavelength, digitized, and averaged over 30 laser shots. The data is then stored on a computer (PC/XT) for further analysis. If not otherwise stated, the reported errors include statistical and experimental uncertainties and represent 1σ deviation.

B. Flame

The atmospheric-pressure oxyacetylene flame consists of a standard welding torch fitted with a 0.94 mm diameter nozzle operated in the open air. The flows of acetylene and oxygen are maintained with mass flow controllers (MKS) at 380 and 360 cc/min, respectively. This results in an oxygen to acetylene volumetric flow ratio, O_2/C_2H_2, of 0.947 and an equivalence ratio, Φ, of 2.64 (fuel rich). The temperature is 2774 ± 140 K at 0.4 mm above the burner nozzle and the CH

concentration is estimated to be 30 ppm.[12] At these concentrations ($\sim 8 \times 10^{11}$ molecules/cm^3 per quantum state) no CH absorption ($<1\%$) is observed.

C. CH Spectral features and collisional rates

Figure 2 shows a DFWM spectrum of the CH radical taken at 0.4 mm above the burner nozzle. The integrated signal intensities of the well-resolved $(0,0)$ band transitions of the A $^2\Delta - X$ $^2\Pi$ system[26] are used in our analysis. The $A-X$ system is highly diagonal,[27-29] and both the X and A states rapidly approach Hund's case (b) coupling as rotation increases. The radiative lifetimes of the $v'=0$ level of the A $^2\Delta$ state are nearly independent of rotational level.[30,31] In recent calculations, however, Luque and Crosley[29] show that there is approximately a 4% variation in the radiative lifetimes for N' quantum numbers ranging from $N'=2$ to $N'=20$. Therefore, we use the calculations of Luque and Crosley and the rotational line strengths of Kovács[32,33] to calculate the Einstein absorption coefficients used in our analysis.[34] Experimental term energies[35] are used for J'' quantum number values up to 12.5. Term energies for higher J'' values are calculated using the spectroscopic constants of Ref. 35.

High-temperature collisional data for the A $^2\Delta(v'=0)$ state of the CH radical are shown in Table I.[36-41] In Table I, R refers to rotational energy transfer and Q refers to quench-

TABLE I. CH energy transfer rates.

Ref.	CH Source	Temperature	N'	R/Q	Q^a
36	Flame	2000 K	11	4^b	5.1 ± 0.4
37	Flame	2040 K	6, 14	$2.4\pm0.1, 4.1\pm0.4$	...
38	Pyrolysis	1300 K	Average	...	5.6 ± 0.4
39	Flame	1600 K	6	3.6 ± 0.5	3.6 ± 2.4
39	Flame	1600 K	3, 12	$2.7\pm0.5, 3.8\pm0.5$	...
40	Flame	1800 K	Average	...	4.7 ± 0.3
41	Flame	1700 K	Average	...	1.8 ± 0.4^c

^{a}Estimated for CH at 2774 K in units of 10^8 s^{-1}.
^{b}Error not reported.
^{c}Estimated error.

ing. Electronic and vibrational energy transfer are not included because these rates are negligible compared to R and Q.[37] When only cross sections are reported, those of CO and H_2 are used to calculate the rate coefficient. These two molecules are considered because Matsui, Yuuki, and Sahara[42] have determined by mass-spectrometric analysis that the reaction zone of oxyacetylene torch burners consists primarily of CO and H_2. The total collisional transfer rate coefficient T_{ij} (s^{-1}) from energy level i to energy level j of species p due to collisions with several species labeled q is given by

$$T_{ij} = \sum_q N_q \bar{\nu}_{pq} \sigma_{ij}^{pq} \qquad (1)$$

where N_q is the number density (molecules/cm^3) of species q, σ_{ij}^{pq} is the cross section (cm^2), and $\bar{\nu}_{pq}$ is the average relative speed (cm/s) of species p and q. The average relative speed is given by

$$\bar{\nu}_{pq} = \left(\frac{8 k_B T}{\pi \mu_{pq}} \right)^{1/2}, \qquad (2)$$

where k_B is the Boltzmann constant, T is the temperature, and μ_{pq} is the reduced mass for species p and q. To our knowledge the highest temperature data available are at 2000 K. The temperatures of interest in our investigations are approximately 2774 K. Therefore, the rates are scaled to this temperature by making a $1/T$ density correction and a $T^{1/2}$ velocity correction. Such a method is accurate if the cross sections do not change significantly with velocity. Strictly speaking, the T_{ij} (s^{-1}) have units of a first-order chemical kinetic rate coefficient; however, they are more commonly referred to as rates in nonlinear optics. Therefore, in what follows we will refer to the collisional transfer rate coefficients T_{ij} as rates.

D. Saturation measurements

In our previous paper[12] saturation measurements were performed by obtaining spectral scans at specific laser intensities. The line-center signal intensities (peak heights) were easily distinguished from the baseline noise. Because of the time required to take a spectral scan at each laser intensity the data accumulation time was quite long (~2 h). We observe for our present experimental conditions that the major source of noise is scattered light. We are not able to observe a coherent nonresonant background signal in these experi-

ments. Furthermore, the scattered light results primarily from beam 2 (probe) because it scatters light directly along the detection axis. A lesser contribution from beam 3 (backward pump) is also observed due to distortion and refraction of the beam after passing through the flame. Scattered light from beam 1 (forward pump) is found to be on the order of the electronic noise of the detection system, which is much less than the noise from the scattered light of beams 2 and 3.

In the present paper we vary the laser energy with the laser frequency held at line center. Specifically, the KrF excimer laser trigger is phase locked with the 50 kHz oscillations of the photoelastic modulation crystal. Varying the laser trigger delay varies the retardation of the light exiting the crystal, and hence, the amount of light that passes through the second polarizer. The laser energy is varied under computer control, and the total light intensity reaching the detector and laser energy are recorded each laser shot. Then in a separate scan the forward pump beam is blocked, and a scattered light signal is obtained as a function of laser energy. Both traces are sorted as a function of laser energy (corrects for shot-to-shot fluctuations) and binned at intervals of 0.5 μJ. The upper and lower solid symbol traces in Fig. 3 are examples of the total signal and scattered light signal, respectively. The scattered light signal (linear in laser energy) is subtracted from the total signal to obtain the DFWM signal as a function of laser energy (open symbols in Fig. 3). This method allows an entire saturation curve to be obtained in approximately 5 min with each data point consisting of an average of 60–90 laser shots.

In calculating the laser spectral intensity from the measured beam energies, we use $\Delta \bar{\nu}_L = 0.18 \pm 0.02$ cm^{-1}, $\Delta \tau_L = 16.3 \pm 1$ ns, and $A = \pi (d_{TH}/2)^2$ where d_{TH} is the "top hat" diameter of a Gaussian beam[43] (d_{TH} equals $1.2 d_{fwhm}$ and typically $d_{fwhm} = 0.5$ mm). For example, typical beam energies employed in these experiments are 16μJ for the forward and backward pump beams and 4μJ for the probe beam. These values correspond to 1.93 and 0.48 MW/cm^2-cm^{-1}, respectively. In what follows I_{sat}^0 is the theoretical line-center saturation intensity, I_{sat}^{ex} is the experimental line-center saturation intensity, and $\langle I_{sat}^{ex} \rangle$ is the average experimental line-center saturation intensity for different polarization configurations of a single transition.
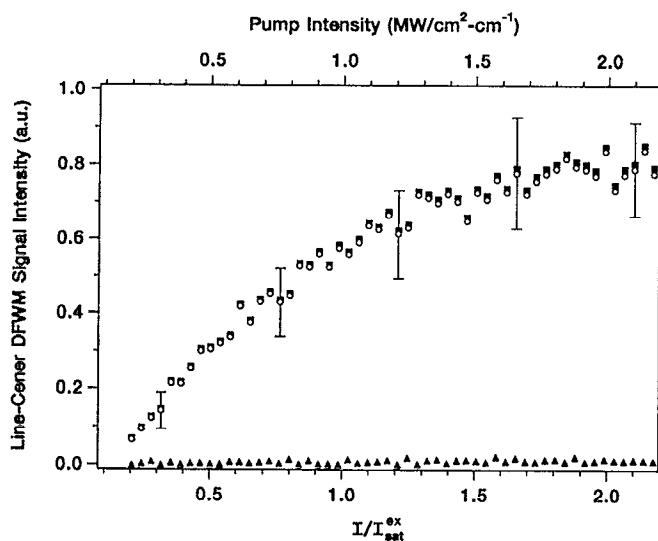
FIG. 3. Line-center saturation curve for the $YYXX$ linear polarization configuration of the $Q_{1ef}(8)$ transition as a function of saturation intensity (bottom), and pump field spectral intensity (top). The upper and lower solid symbol traces in the figure are the total signal (-■-) and scattered light (-▲-) signal, respectively. The scattered light signal (linear in laser intensity) is subtracted from the total signal to obtain the DFWM signal as a function of laser intensity (-O-).

E. Polarization measurements

The experiment is configured so that any linear polarization configuration is obtained by rotating the half-wave plates shown in Fig. 1. After polarization rotation each pump beam is directed by one additional mirror. Differences in S and P reflectance for all the mirrors is approximately 3%. The beam splitter in the probe axis, which is used to collect the DFWM signal, reflects P-polarized light at 66.4%±6% times the efficiency for S-polarized light. The probe mirror, however, reflects P-polarized light at a higher efficiency than S-polarized light which results in less than 5% difference in the probe field intensity at the flame as its polarization is rotated. The polarization purity of all of the electric fields is greater than 98%.

Shot-to-shot polarization measurements are performed by placing the photoelastic modulator in place of one of the half-wave plates and removing the polarizer from the detection axis. The laser delay relative to the photoelastic modulator is adjusted on a shot-to-shot basis so that every other shot corresponds to either 0° or 180° retardation (half-wave plate). The DFWM signal and laser energy are averaged over 30 laser shots for each polarization configuration and for each spectral position. The shot-to-shot measurements enable polarization ratios to be obtained in real time at a single laser intensity. These measurements are used to check the accuracy of polarization measurements taken a few minutes apart.

In what follows Y represents the linear polarization state that corresponds to S-polarized light, i.e., light polarized perpendicular to the plane of the laser table, and X represents P-polarized light. In addition we use the notation established in WZR1 where a polarization configuration is given as $\epsilon_4\epsilon_1\epsilon_3\epsilon_2$ where ϵ_j is the polarization vector of the electric

field labeled j. For example the $YYXX$ polarization configuration corresponds to E_4 and E_1 being Y polarized and E_3 and E_2 being X polarized.

F. Rotational temperature measurements

In our rotational temperature analysis resolved Q_1 and Q_2 transitions of the CH $A\ ^2\Delta - X\ ^2\Pi$ (0,0) band are used. For CH the Q branch covers a small spectral region and is sufficiently resolved to allow the analysis of individual DFWM transitions. Therefore, rotational temperatures are obtained with minimal scan times. The $XXXX$ and $YXYX$ polarization configurations have been used in previous experiments.[3,6–12] but we chose the $YYXX$ configuration because it offers many advantages. First the $YYXX$ polarization configuration greatly discriminates against thermal grating contributions because only small-spaced intensity gratings are present.[5,44] We have not observed any direct evidence to suggest that thermal gratings are produced in this flame; however, this polarization configuration assures that their interference is negligible. Second, as stated in Sec. II D, the primary source of noise in these experiments is scattered light from the probe beam ($\sim$90%) and the backward pump beam ($\sim$10%) with a negligible contribution (on the order of the electronic noise) from the forward pump beam. In the $YYXX$ polarization configuration, the signal beam is crossed polarized to both of the "noisy" beams, and therefore the $YYXX$ configuration offers true zero background detection when a linear polarizer is placed in the detection axis. Contrary to first impressions, the PC-DFWM signal intensity using the $YYXX$ polarization configuration is equal to the $YXYX$ configuration. Both these configurations give approximately 1/9 the signal intensity of the $XXXX$ configuration (WZR1, Table III), but the thermal-grating and scattered-light discrimination make up for the loss of signal.

III. SATURATION MODELS

The AL model considers a nondegenerate two-level homogeneously broadened system in the presence of arbitrary pump field intensities and weak probe and signal intensities. In this model all fields are assumed to be monochromatic. In the limit of weak probe and signal intensities a full solution of the density matrix equation for the interaction of the pump fields with the two-level system is possible. The density matrix solution for two-level nondegenerate saturable absorbers in the presence of arbitrary field intensities is well known in semiclassical laser theory. An excellent discussion of the topic is given in Ref. 45.

For electric fields defined as

$$\mathbf{E}_j(z,t) = \frac{1}{2}\,\mathbf{E}_j e^{-i(\omega_j t - k_j z)} + \text{c.c.}; \quad \mathbf{E}_j = \mathscr{E}_j \epsilon_j;$$

$$I_j = \frac{c\epsilon_0}{2}\,|\mathscr{E}_j|^2, \tag{3}$$

where $\mathbf{E}_j$ is the vector amplitude, $\mathscr{E}_j$ is the scalar amplitude, ϵ_j is the normalized ($\epsilon_j \cdot \epsilon_j^* = 1$) polarization unit vector, and I_j is the intensity of the electric field labeled j, the den-

sity matrix solution in the rotating-wave approximation for the steady-state population (number density) difference $\Delta N = N_g - N_e$ is

$$\Delta N = \frac{\Delta N_0}{1 + n|\Omega|^2/|\Omega_{\text{sat}}|^2} = \frac{\Delta N_0}{1 + nI/I_{\text{sat}}^0}, \tag{4a}$$

with

$$n = \frac{4 \cos^2(kz)}{1 + (\Delta/\Gamma_{eg})^2}. \tag{4b}$$

The Rabi frequency $|\Omega_j|$ associated with the field labeled j is defined with respect to the field intensity I_j as

$$|\Omega_j|^2 = \frac{|\mu_{ge}\mathscr{E}_j|^2}{\hbar^2} = \frac{2|\mu_{ge}|^2}{c\epsilon_0\hbar^2} I_j, \tag{5}$$

and the saturation Rabi frequency $|\Omega_{\text{sat}}| = (\Gamma_0\Gamma_{eg})^{1/2}$ is defined with respect to the line-center saturation intensity I_{sat}^0 as

$$|\Omega_{\text{sat}}|^2 = \frac{2|\mu_{ge}|^2}{c\epsilon_0\hbar^2} I_{\text{sat}}^0. \tag{6}$$

In Eqs. (4)–(6) g refers to the lower level, e refers to the upper level, $\Delta N_0 = N_g^0 - N_e^0$ is the population difference of the two-level system in the absence of applied fields, $|\mu_{ge}|^2$ is the square of the transition dipole moment connecting levels g and e, $|\Omega|$ is the Rabi frequency associated with the pump fields ($|\Omega| = |\Omega_1| = |\Omega_3|$), I is the intensity of the pump fields ($I = I_1 = I_3$), k is the magnitude of the propagation vector of the fields, $\Delta = \omega - \omega_0$ is the spectral shift from the resonance frequency ω_0, and Γ_0 and Γ_{eg} are the population relaxation and coherence dephasing rates, respectively. All of the terms are in SI units, and the constants ϵ_0, $\hbar$ and c have their usual meanings.

In Eq. (4) we see that the result of the interference of the two counterpropagating pump fields is a sinusoidally varying electric field intensity that spatially "burns holes" into the population difference spaced one-half wavelength apart.[46] The two-level system is said to be saturated when the population difference, $\Delta N = N_g - N_e$, is zero over the entire interaction volume. Inspection of Eqs. (4) and (6) shows that saturation occurs when the optical pumping rate denoted by the Rabi frequency is much faster than the population relaxation and coherence dephasing rates.

Having obtained the system response in the presence of strong pump fields, perturbation theory is used to include the weak probe and signal fields. The final result is an analytic model of the DFWM signal. AL solved the slowly varying envelope approximation (SVEA) equations for the probe and signal fields. In the limit of no absorption, the SVEA equations are

$$\frac{d\mathscr{E}_2}{dz} = 0, \quad \frac{d\mathscr{E}_4}{dz} = i\beta\mathscr{E}_2^*, \tag{7}$$

where β is the nonlinear coupling coefficient defined in Ref. 2, Eq. (16). For the case of equal intensity pumps, the expression for the DFWM signal[2,47,48] is given by

$$I_{\text{DFWM}} = |\beta|^2 L^2 I_2 = R_{\text{AL}} I_2, \tag{8}$$

with

$$R_{\text{AL}} = 4\alpha_0^2 L^2 \left[\frac{I}{I_{\text{sat}}^0}\right]^2 \left[\frac{\Gamma_{eg}^2}{\Delta^2 + \Gamma_S^2}\right]^3, \tag{9}$$

$$\alpha_0 = \frac{\omega_0\Delta N_0|\mu_{ge}|^2}{2c\epsilon_0\hbar\Gamma_{eg}}, \tag{10}$$

and

$$\Gamma_S = \Gamma_{eg}(1 + 4I/I_{\text{sat}}^0)^{1/2}. \tag{11}$$

In Eqs. (8)–(11) R_{AL} is the AL model reflectivity, α_0 is the line-center attenuation coefficient, L is the effective interaction length of the excitation fields, $I = I_1 = I_3$ is the intensity of the pump fields, and I_2 is the intensity of the probe field. Equation (8) defines the cube of a power-broadened Lorentzian with an actual half-width given by $\Gamma_S(2^{3/2} - 1)^{1/2}$.

The formulation of the MCECA model is similar in concept to the AL model with the exception that the excitation fields are not monochromatic (coherent). The MCECA model considers a medium of two-level nondegenerate absorbers transversed by two broad-bandwidth (incoherent) copolarized pump fields of equal and arbitrary intensity and a weak probe field of any bandwidth. Furthermore MCECA assume that the fields are statistically independent (chaotic) and uncorrelated (delayed with respect to each other by a distance much greater than the coherence length).[49-51] The bandwidths of the pump fields have a Lorentzian spectral shape with a FWHM of $\Delta\omega_1 = \Delta\omega_3 = 2b$. Most importantly, this model assumes that the bandwidths exceed all other rates that determine the time evolution of the system, i.e., $b \gg |\Omega|, \Gamma_0, \Gamma_{eg}$. In this case the bandwidth-dependent saturation Rabi frequency is given by $|\Omega_{\text{sat}}| = (b\Gamma_0)^{1/2}$, and the average density matrix population terms vary on a time scale of $1/\Gamma_0$ whereas the much shorter correlation time of the fields varies as $1/b$. Under these conditions, all products of field and population terms may be treated as uncorrelated. This aspect is the key element of the treatment.

In contrast to the AL model expression of Eq. (4) which involves coherent fields, the interference of the counterpropagating pump fields considered by MCECA does not produce a steady-state standing wave pattern because the fields are incoherent and uncorrelated. Replacing the $\cos^2(kz)$ term of Eq. (4b) with its average value of 1/2 and assuming that $b \gg \Gamma_{eg}$, we obtain the expression for the steady-state population difference $\Delta N = N_g - N_e$ of the MCECA model, namely,

$$\Delta N = \frac{\Delta N_0}{1 + m|\Omega|^2/|\Omega_{\text{sat}}|^2} = \frac{\Delta N_0}{1 + mI/I_{\text{sat}}^0}, \tag{12a}$$

with

$$m = \frac{2}{1 + (\Delta/b)^2}, \tag{12b}$$

where I_{sat}^0 is defined by Eq. (6) with $|\Omega_{\text{sat}}|^2 = b\Gamma_0$. We see in Eq. (12) that stronger fields are required to saturate the two-level system when broad-bandwidth lasers are used because the Rabi frequency must now exceed $(b\Gamma_0)^{1/2}$ which is much larger than $(\Gamma_0\Gamma_{12})^{1/2}$.

Analytic expressions[14] for the DFWM signal of the MCECA model are obtained when the bandwidth of the

probe field, $\Delta\omega_2=2p$, is also large in the sense that $|\Omega|^2 \ll pb$ and $p \gg \Gamma_0, \Gamma_{eg}$. Specifically for $p=b$ and for small detunings compared to the laser bandwidth ($\Delta \ll b$), we have the simplified MCECA expression for the DFWM signal, namely,

$$I_{\text{DFWM}} = R_{\text{MCECA}} I_2,$$ (13)

where

$$R_{\text{MCECA}} = \frac{\Gamma_0}{b} \alpha_0^2 L^2 \left[\frac{I}{I_{\text{sat}}^0}\right]^2$$

$$\times \left[\frac{\Delta^2+b^2}{\Delta^2+\Gamma_{S1}^2}\right]^{1/2} \left[\frac{b^4}{(\Delta^2+\Gamma_{S2}^2)(\Delta^2+\Gamma_{S3}^2)}\right]^{3/2},$$ (14)

$$\Gamma_{S1} = b(1+r_{\text{pc}}I/I_{\text{sat}}^0)^{1/2},$$ (15)

$$\Gamma_{S2} = b(1+2I/I_{\text{sat}}^0)^{1/2},$$ (16)

and

$$\Gamma_{S3} = b(1+(2+r_{\text{pc}})I/I_{\text{sat}}^0)^{1/2}.$$ (17)

In Eqs. (13)–(17) r_{pc} is the ratio of the population relaxation rate to the coherence dephasing rate ($r_{\text{pc}}=\Gamma_0/\Gamma_{12}$), and the remaining terms have been defined previously. For $I \leq 3I_{\text{sat}}^0$, Eq. (13) approximates a power-broadened Lorentzian-cubed profile like the AL model but with a spectral width determined by the laser bandwidth. For higher laser intensities, the line shape power broadens more rapidly than a Lorentzian-cubed profile and develops a dip at line center. The intensity range over which Eq. (13) applies depends on the laser bandwidth and the population relaxation rate caused by the environment. Because $b \gg |\Omega|$ and $|\Omega_{\text{sat}}|^2 = b\Gamma_0$, we find that the condition

$$I/I_{\text{sat}}^0 = |\Omega|^2/|\Omega_{\text{sat}}|^2 \ll b/\Gamma_0$$ (18)

needs to be satisfied for Eq. (13) to be valid.

The collisional relaxation and dephasing rates for our experimental conditions must be determined in order to apply the models discussed in this section. We base the discussion on the available relaxation data for the CH radical (Sec. II C), but the discussion is also applicable to other flame and plasma species. For molecules in collisionally dominated environments, the rotational levels involved in the one-photon transition are effectively coupled by rotational energy transfer (R) collisions to other rotational levels. Furthermore, the excited rotational levels are coupled to the ground rotational levels by quenching (Q) and spontaneous emission (A_{eg}). For this case the relaxation of the molecular levels approximates a four-level system.[52] For such a system the population relaxation and coherence dephasing rates are defined[45] as

$$\Gamma_0 = \frac{2\Gamma_g \Gamma_e}{(\Gamma_g+\Gamma_e)},$$ (19)

and

$$\Gamma_{eg} = \tfrac{1}{2}(\Gamma_g+\Gamma_e)+\Gamma_{eg}^{pd},$$ (20)

where Γ_g and Γ_e are the population relaxation rates of levels g and e, and Γ_{eg}^{pd} is the pure dephasing rate of the dipolar transition.

In our analysis we take R to be the same for the $A\,^2\Delta(\nu'=0)$ and $X\,^2\Pi(\nu''=0)$ levels because the rotational spacings are very similar and define the ground and excited population relaxation rates as $\Gamma_g=R$ and $\Gamma_e=R+Q+A_{eg}$, respectively. With these definitions we estimate an average population relaxation rate of $\Gamma_0=2\times10^9$ s^{-1} using the values of Table I. Assuming that the pure dephasing rate is small compared to R, we have $\Gamma_0 \cong \Gamma_{eg}$ ($r_{\text{pc}}=0.98$ for $R/Q=3.5$). Furthermore, because the characteristic collisional relaxation times are ~32 times shorter than the laser pulse, i.e., $\Delta\tau_L \gg 1/\Gamma_g \cong 1/\Gamma_e$, steady-state conditions are assumed, and we use the AL and MCECA expressions discussed in this section.[53] In addition we expect the MCECA model to apply for laser intensities up to approximately twice the saturation intensity because $b/\Gamma_0=9$ in Eq. (18). In Eqs. (8) and (13) ΔN_0 is replaced with the ground state population because $N_g^0 \gg N_e^0$ for our flame conditions.[12]

IV. RESULTS AND DISCUSSION

A. Polarization ratios as a probe of collisional dynamics

In WZR1 we discussed how DFWM polarization measurements provide information about the collisional relaxation caused by the environment. Line-center saturation curves like those of Fig. 3 for the $R_{1f}(8)$ and $Q_{1ef}(8)$ transitions were obtained for different linear polarization configurations. The line-center saturation curves of the $R_{1f}(8)$ transition are shown in Fig. 4. The absolute signal intensities dramatically differ for the four polarization configurations. To emphasize the differences in signal intensities, polarization ratios as a function of laser intensity are made from the saturation curves. Figure 5 shows polarization ratios of the $R_{1f}(8)$ and $Q_{1ef}(8)$ transitions as a function of pump field intensity. The solid symbols in Fig. 5 are experimental data and dashed lines in Fig. 5 are the predicted polarization ratios using WZR1, Table III.

Figure 5(a) shows the $XYYX/XXXX$ polarization ratio of the $R_{1f}(8)$ transition, and Fig. 5(b) shows the $YYXX/YXYX$ polarization ratio of the $Q_{1ef}(8)$ transition. The predicted polarization ratios in Figs. 5(a) and 5(b) are in good agreement with the data at weak pump field intensity. Specifically, the average value of the data between 0.1 and 0.4 $\langle I_{\text{sat}}^{\text{ex}} \rangle$ is 0.20 ± 0.06 in Fig. 5(a) and 0.92 ± 0.14 in Fig. 5(b). These values are close to the predicted polarization ratios of 0.24 and 1.0, respectively. Recall that the values of WZR1, Table III were derived assuming that all of the multipole moments of the total angular momentum distribution, i.e., the population, the orientation, and the alignment, relax at the same rate and that no other process contributes to the observed signal.

We have observed Q-branch polarization ratios different from the values of WZR1, Table III for the OH radical in the burnt gas region of atmospheric-pressure hydrogen–oxygen flames.[54,55] We have attributed this effect to the presence of thermal gratings. With helium dilution, however, thermal
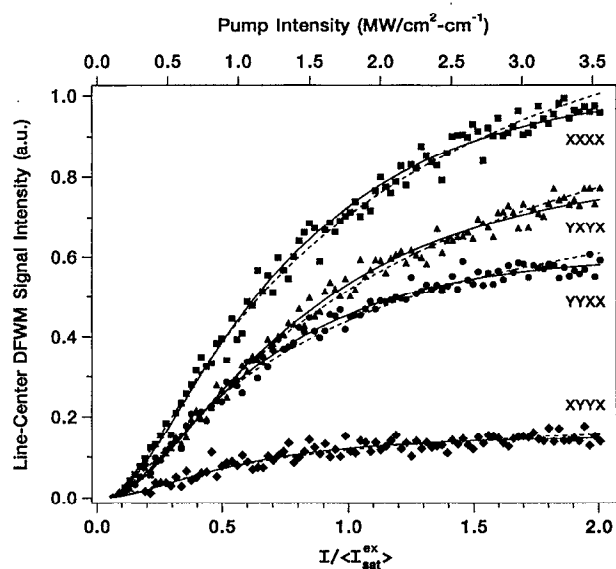
FIG. 4. Line-center saturation curves for different linear polarization configurations of the $R_{1f}(8)$ transition as a function of average saturation intensity $\langle I_{sat}^{ex} \rangle = 1.77$ MW/cm^2–cm^{-1} (bottom), and pump field spectral intensity (top). In the figure -■-, -▲-, -●- and -♦- correspond to the $XXXX$, $YXYX$, $YYXX$, and $XYYX$ polarization configurations, respectively. The absolute signal intensities dramatically differ for the four polarization configurations, but the saturation intensities (Table II) obtained from the AL model (dashed curves) and MCECA model (solid curves) are nearly equal for all polarization configurations.

gratings are no longer present, but anomalous polarization ratios are still observed for levels with low J quantum numbers. Nearly degenerate four-wave mixing (NDFWM) scans confirmed that in the helium-diluted flames the rates of relaxation of the multipole moments are not equal.[56] Therefore the good agreement between the data at low intensity in Figs. 5(a) and 5(b) with the calculated values implies that the mutipole moments are relaxing equally and that other laser-induced phenomena such as a thermal grating are not present.

In PC-DFWM of Doppler-broadened systems, polarization ratios of P- and R-branch transitions are dependent on the relative values of the relaxation rates of ground and excited levels when the pump fields are cross polarized, i.e., when the $YYXX$ and $YXYX$ polarization configurations are used. We estimate a collisional full width, $2\Gamma_{eg}$, of 4×10^9 s^{-1} (0.02 cm^{-1}) and a Doppler width, $\Delta\omega_D$, of 46×10^9 s^{-1} (0.24 cm^{-1}) for CH at 2774 K. Our experiment corresponds to a Doppler-broadened system because $\Delta\omega_D > 2\Gamma_{eg}$. For such a system the $YYXX/YXYX$ polarization ratio of the $R_{1f}(8)$ transition has a value of 1.4 when $\Gamma_e \ll \Gamma_g$, 0.70 when $\Gamma_e \gg \Gamma_g$, and 1.0 when $\Gamma_e = \Gamma_g$.

Figure 5(c) illustrates the $YYXX/YXYX$ polarization ratio for the $R_{1f}(8)$ transition, and the dashed line of Fig. 5(c) is the prediction of WZR1, Table III which corresponds to $\Gamma_e = \Gamma_g$. The average value of the data between 0.1 and 0.4 $\langle I_{sat}^{ex} \rangle$ is 1.04 ± 0.09 which suggests that the relaxation rates of the ground and excited levels are approximately equal. This conclusion is consistent with the energy transfer data available for the CH radical. The rotational spacings of the $\nu = 0$
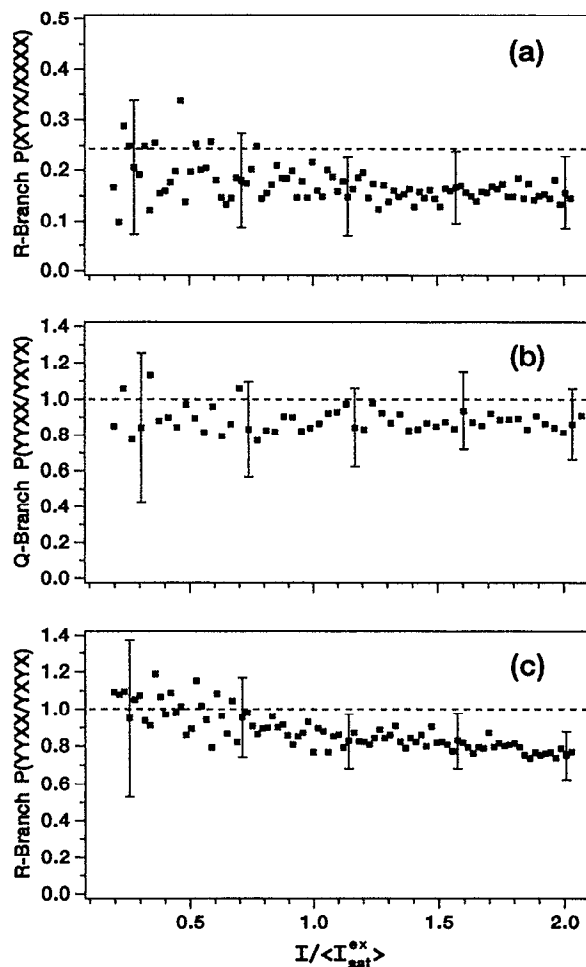

FIG. 5. The solid points are the experimental polarization ratios and the dashed lines are the predicted polarization ratios using WZR1, Table III. (a) $XYYX/XXXX$ polarization ratio for the $R_{1f}(8)$ transition as a function of average saturation intensity $\langle I_{sat}^{ex} \rangle = 1.77$ MW/cm^2–cm^{-1}. The average value of the data between 0.1 and 0.4 $\langle I_{sat}^{ex} \rangle$ is 0.20 ± 0.06 which is in good agreement with the calculated value of 0.24. (b) $YYXX/YXYX$ polarization ratio for the $Q_{1ef}(8)$ transition as a function of average saturation intensity $\langle I_{sat}^{ex} \rangle = 1.10$ MW/cm^2–cm^{-1}. The average value of the data between 0.1 and 0.4 $\langle I_{sat}^{ex} \rangle$ is 0.92 ± 0.14 which is close to the expected value of 1.0. (c) $YYXX/YXYX$ polarization ratio for the $R_{1f}(8)$ transition as a function of average saturation intensity $\langle I_{sat}^{ex} \rangle = 1.77$ MW/cm^2–cm^{-1}. The average value of the data between 0.1 and 0.4 $\langle I_{sat}^{ex} \rangle$ is 1.04 ± 0.09 which is close to the expected value of 1.0.

vibrational levels of the X and A states of CH are nearly same, and the rotational energy transfer rate of the $\nu' = 0$ level of the A state is approximately 3.5 times faster than quenching. Furthermore, if the quenching collisions do not trap population in higher vibrational states (rapid energy transfer to $\nu'' = 0$), we expect that $\Gamma_g \cong \Gamma_e$ according to the four-level model referred to in Sec. III.

The most significant aspect of Fig. 5 is that the experimental polarization ratios are slowly varying with laser intensity and are within 30% of the perturbative calculations up to twice the saturation intensity. In the weak-field limit the DFWM signal is dependent on the spatial anisotropy of the total angular momentum distribution induced by the three

TABLE II. Experimentally determined line-center saturation intensities.

Transition	$\epsilon_4\epsilon_1\epsilon_3\epsilon_2$	AL I_{sat}^{ex} (MW/cm^2–cm^{-1})	MCECA I_{sat}^{ex} (MW/cm^2–cm^{-1})
$Q_{1ef}(4)$	$YYXX$	1.88 ± 1.19	1.76 ± 0.74
$R_{1f}(4)$	$YYXX$	2.47 ± 0.83	2.21 ± 0.54
$Q_{1ef}(8)$	$YXYX$	1.06 ± 0.38	1.12 ± 0.25
$Q_{1ef}(8)$	$YYXX$	1.00 ± 0.51	1.08 ± 0.32
$R_{1f}(8)$	$XXXX$	1.88 ± 0.33	1.79 ± 0.21
$R_{1f}(8)$	$YXYX$	2.30 ± 0.43	2.07 ± 0.29
$R_{1f}(8)$	$YYXX$	1.68 ± 0.41	1.72 ± 0.25
$R_{1f}(8)$	$XYYX$	1.21 ± 1.34	1.51 ± 0.81

input fields. Therefore, this close agreement implies that the relative anisotropy of the total angular momentum represented by the total geometric factors persists to a large degree as the laser intensity increases. This effect is similar to that expected for saturated laser induced fluorescence measured with different polarization configurations (Fig. 5 of Ref. 57).

B. Saturation behavior

The line-center saturation intensities resulting from nonlinear least squares fits of saturation data to the power dependencies of the AL model, Eq. (8) and the MCECA model, Eq. (13) for $\Delta=0$ and $r_{pc}=0.98$ are given in Table II. In Table II, the total error increases significantly as the ratio of the DFWM signal to the scattered light intensity decreases. The AL model and the MCECA model exhibit very similar saturation behavior for moderately high laser intensities $(I \sim I_{sat}^0)$. This statement is validated by the fact that the fitted saturation curves (Fig. 4) and saturation intensities (Table II) of the two models are very similar. Therefore, it is not surprising that the AL model has been able to qualitatively reproduce the saturation behavior for experiments employing broad-bandwidth (multimode) lasers.[12] The error associated with the MCECA saturation intensities, however, is approximately 30% smaller than the error associated with the AL saturation intensities. The reduced error results from the fact that the fits to MCECA model are more sensitive to the value of the saturation intensity (higher order power dependence) and are better correlated with the data.

For a single transition, the fitted MCECA saturation intensities of Table II are approximately equal regardless of the polarization configuration. For instance, the saturation intensities for the four polarization configurations of the $R_{1f}(8)$ transition are within 30% of the average value $\langle I_{sat}^{ex}\rangle$ of 1.77 MW/cm^2–cm^{-1}. This similarity is more easily seen in Fig. 6 which shows the DFWM reflectivity at line center for the four polarization configurations of the $R_{1f}(8)$ transition. The MCECA line-center reflectivity is at a maximum at 0.6 I_{sat}^0, and in Fig. 6, the reflectivity for each polarization configuration peaks at approximately the same pump field intensity. This effect is independent of the fact that the absolute magnitude of the reflectivities differ for the various polarization configurations.

We suggest the following explanation for the weak sensitivity of the DFWM saturation intensity to polarization. In
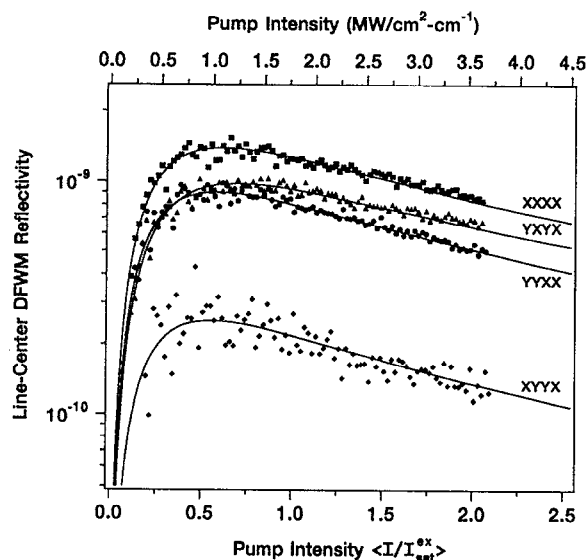

FIG. 6. Line-center reflectivity curves for different linear polarization configurations of the $R_{1f}(8)$ transition as a function of average saturation intensity $\langle I_{sat}^{ex}\rangle=1.77$ MW/cm^2–cm^{-1} (bottom), and pump field spectral intensity (top). In the figure -■-, -▲-, -●-, and -◆- correspond to the $XXXX$, $YXYX$, $YYXX$, and $XYYX$ polarization configurations, respectively. The solid curves are nonlinear least squares fits of the data to the MCECA model, Eq. (14). All of the reflectivity curves peak at approximately the same pump field intensity.

the framework of the MCECA model discussed in Sec. III, the DFWM signal saturates when the population difference of Eq. (12) induced by the counterpropagating pump fields approaches zero over the entire interaction volume. At this point the probe field cannot perturb the population (make gratings) and the DFWM reflectivity approaches zero. The intensity at which the spatial population difference of the two-level system approaches zero is determined by I_{sat}^0. Because $I_{sat}^0 \propto b\Gamma_0/|\mu_{ge}|^2$ for the MCECA model, this intensity is related to the collisional relaxation caused by the environment and the Einstein absorption coefficient $[|\mu_{ge}|^2=(3\epsilon_0\hbar^2/\pi)B_{ge}]$. For a nondegenerate two-level system this intensity is unambiguous.

The transition probabilities for a molecular (degenerate) transition, however, are dependent on the magnetic sublevels involved, the type of transition, and polarization state of the excitation field. In other words, for a given transition and field polarization, some magnetic sublevels interact strongly with the field and others do not. Those sublevels interacting strongly with the field saturate more rapidly than those that do not. Therefore, to describe the saturation properties of a molecular system each magnetic sublevel must be treated independently, i.e., there is no single Rabi frequency for a degenerate system.[58] It is common in rate equation models of molecular processes, however, to use Einstein A and B coefficients[57] which represent an equally weighted average of the transition probabilities of all the magnetic sublevels.[34,58–60] Furthermore, if the initial magnetic sublevel distribution is isotropic the average optical pumping rate, i.e., the rms Rabi frequency, is independent of the field polarization.[58]

Therefore, to a first approximation the average intensity at which the population difference approaches zero will be related to the Einstein absorption coefficient. Furthermore, we expect this intensity to be similar for the different polarization cases provided that the magnetic sublevels relax with equal rates, i.e., if the population, orientation, and alignment relax equally.[24] In Sec. IV A we showed this to be a reasonable assumption for CH in this flame. The saturation data presented in Table II validates this expectation because the saturation intensities for different polarization configurations involving the same transitions are similar; the values are within a factor of 2 of one another. In addition the ratio of the $Q_{1ef}(4)$ and $R_{1f}(4)$ saturation intensities is 0.80 ± 0.39, and the ratio of the $Q_{1ef}(8)$ and $R_{1f}(8)$ saturation intensities is 0.63 ± 0.21. These values are close to the inverse ratio of the B_{ge} coefficients for these transitions of 1.01 and 0.71, respectively. Note that the polarization dependence of the Q- and R-branch transitions differ sharply. In constructing these saturation ratios we used the $YYXX$ saturation intensities of the MCECA model, chose transitions that shared a common ground level, and assumed that effects arising from differences in the excited level degeneracies and collisional rates are small.

C. Numerical comparisons

The calculated AL and MCECA saturation intensities for the $R_{1f}(8)$ transition using $\Gamma_0 = \Gamma_{12} = 2 \times 10^9$ s^{-1} and $|\mu_{ge}| = 0.405$ D are 0.0031 and 0.028 MW/cm^2, respectively. The bandwidth-corrected MCECA saturation intensity is approximately an order of magnitude larger than the AL saturation intensity; however, the MCECA saturation intensity is still an order of magnitude smaller than our average experimentally determined value of 0.32 ± 0.08 MW/cm^2. Order-of-magnitude agreement was also observed in the MCECA experiments.[13] There are several possible reasons for the discrepancy between the calculated and measured saturation intensities, although no single reason appears to be able to account for such a large difference.

The fact the MCECA model does not include effects arising from the spatial beam properties could account for some of the difference (possibly up to a factor of ten). The LFR calculations discussed in Sec. I, however, showed good agreement with their experimental results using a narrow-bandwidth laser even though the calculations neglected the spatial characteristics of the excitation beams. Therefore, it is unlikely that the Gaussian nature of the excitation beams is solely responsible. The LFR calculations did show, however, that the saturation intensity increases as the ratio $2\Gamma_{eg}$ to $\Delta\omega_D$ decreases. Therefore, the fact that the molecules are moving may account for some of the difference (less than a factor of 2). It is also possible that we have underestimated the values of the relaxation rates by employing the simple $T^{1/2}$ temperature extrapolation and by neglecting the effects of velocity changing collisions. Using larger relaxation rates would increase the calculated saturation intensity (possibly a factor of 2).

Another indication of saturation is power-broadening of line shapes. Figure 7 shows the average DFWM line width (FWHM) of the $R_{1e}(8)$, $R_{1f}(8)$, $R_{2e}(8)$, and $R_{2f}(8)$ transi-
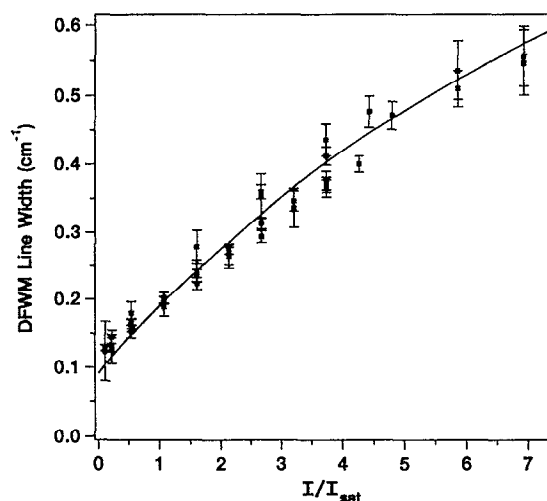

FIG. 7. Average DFWM line width (FWHM) of the $R_{1e}(8)$, $R_{1f}(8)$, $R_{2e}(8)$, and $R_{2f}(8)$ transitions as a function of I/I_{sat}. Each data point represents a separate spectral scan from which an average value was obtained. The solid line is the theoretical MCECA model prediction of Eq. (13) using the laser bandwidth of $\Delta\bar{v} = 0.18$ cm^{-1} and no adjustable parameters. The experimental data is plotted vs I/I_{sat}^{ex} and the theoretical curve is plotted vs I/I_{sat}^0 where I_{sat}^{ex} and I_{sat}^0 are the experimental and theoretical saturation intensities, respectively.

tions as a function of I/I_{sat}. Each data point in Fig. 7 represents a separate spectral scan from which an average value was obtained. The solid line is the theoretical MCECA model prediction of Eq. (13) using the laser bandwidth of $\Delta\bar{v} = 0.18$ cm^{-1} and no adjustable parameters. The experimental data is plotted vs I/I_{sat}^{ex} and the theoretical curve is plotted vs I/I_{sat}^0 where I_{sat}^{ex} and I_{sat}^0 are the experimental and theoretical saturation intensities, respectively. The simplified form of the MCECA model expressed in Eq. (13) is strictly valid for small detunings ($\Delta < b$); however, the agreement of the model with the data is quite good even for laser intensities outside the range of applicability defined in Eq. (18). In addition Eq. (13) approximates a power-broadened Lorentzian-cubed line shape for laser intensities less than 3 I_{sat}, and this line shape reproduces the experimental data.[12] Therefore, an estimate of the degree of saturation of any transition can be determined from the power-broadened linewidth and Eq. (13).

A comparison can also be made between the calculated and measured DFWM reflectivities. Steel and Lamb[2,61] have empirically modified the AL reflectivity expression for homogeneously broadened systems to apply to Doppler-broadened systems, i.e., $\Delta\omega_D \gg 2\Gamma_{eg}$. The resulting expression also showed good agreement with their experimental data. Steel and Lamb express the Doppler-broadened reflectivity, R_D, as

$$R_D \cong \frac{\pi}{16} \frac{(\Gamma_{eg})^2}{(ku)^2} R_{AL}(\Delta = 0), \qquad (21)$$

where u is the most probable speed of the Maxwell–Boltzmann velocity distribution and $R_{AL}(\Delta = 0)$ is the line-center DFWM reflectivity of Eq. (9) for homogeneously

broadened media. We note that Eq. (21) is consistent with the ratio of perturbative expressions [WZR1, Eqs. (46)–(51)] evaluated in the Doppler-broadened limit ($\Delta\omega_D \gg 2\Gamma_{eg}$) and homogeneously broadened limit ($\Delta\omega_D \ll 2\Gamma_{eg}$).[62]

MCECA have also presented an approximate expression for the Doppler-broadened reflectivity [Eq. (22) of Ref. 14]. Comparing that expression to Eq. (14), we find that the Doppler-broadened DFWM reflectivity using broad-bandwidth lasers, i.e., $\Delta\omega_D > 2b \gg 2\Gamma_{eg}$, scales relative to the homogeneously broadened reflectivity as

$$R_D \cong \frac{\sqrt{\pi}}{8} \frac{b\Gamma_{eg}}{(ku)^2} R_{MCECA}(\Delta = 0), \qquad (22)$$

where $R_{MCECA}(\Delta=0)$ is the line-center DFWM reflectivity of Eq. (14) for homogeneously broadened media.

The calculated Doppler-broadened reflectivity for the MCECA model at $I = I_{sat}^0$ and $\Delta = 0$ for the $R_{1f}(8)$ transition is 1.0×10^{-9} using Eqs. (14) and (22). This value is calculated for $T = 2774$ K, $\Gamma_0 = \Gamma_{eg} = 2\times10^9$ s^{-1}, $\Delta N = 1.1\times10^{12}$ molecules/cm^3 [population of the $F_{1f}(8)$ level], $|\mu_{ge}| = 0.405$ D, and $L = 1$ mm (diameter of the flame). The calculated reflectivity is close to the reflectivities measured at the experimental saturation intensity ($I = I_{sat}^{ex}$) which ranged from 0.2 to 1.2×10^{-9} (see Fig. 6). The smallest and largest values in the range correspond to data taken using the $XYYX$ and $XXXX$ polarization configurations, respectively. Because of the numerous calibrations required to evaluate the reflectivity, the measured values are only accurate within a factor of three. Based on the agreement between the calculated and measured reflectivities, Eq. (22) should provide an order-of-magnitude estimate for the feasibility of detecting molecular species in Doppler-broadened media with broad-bandwidth lasers.

D. Relative branch intensities

The spectral scan shown in Fig. 2 was taken using the $YYXX$ polarization configuration at 1.7 times the experimental saturation intensity of the $Q_{1ef}(8)$ transition. Using Eq. (13) we find that the line widths of the transitions shown in Fig. 2 represent a range of approximately 0.9 to $2.3I_{sat}^{ex}$. By varying B_{ge} by $\pm 10\%$ for various I/I_{sat}^0 values and numerically integrating Eq. (13) we find that the MCECA model predicts a $B_{ge}^{2.14}$ to $B_{ge}^{1.71}$ dependence for the integrated DFWM signal over the range of 0.9 to $2.3I_{sat}^0$. This absorption coefficient dependence is consistent with the experimental results of Farrow, Rakestraw, and Dreier.[47] These authors employed a multimode laser similar to that used here and found that the integrated DFWM signal exhibits a reduced absorption coefficient dependence at saturating laser intensities.

We have plotted in Fig. 8 the ratio of the integrated intensities for Q_1 and R_1 transitions that share a common initial state. In plotting the relative branch intensities as a function of J_g we assume that the population relaxation and dephasing rates do not differ significantly even though the Q branch involves J_g and $J_e = J_g$ and the R branch involves J_g and $J_e = J_g + 1$. The dashed curve in Fig. 8 is the B_{ge}^2 saturated two-level (STL) model prediction for the Q-to-R-
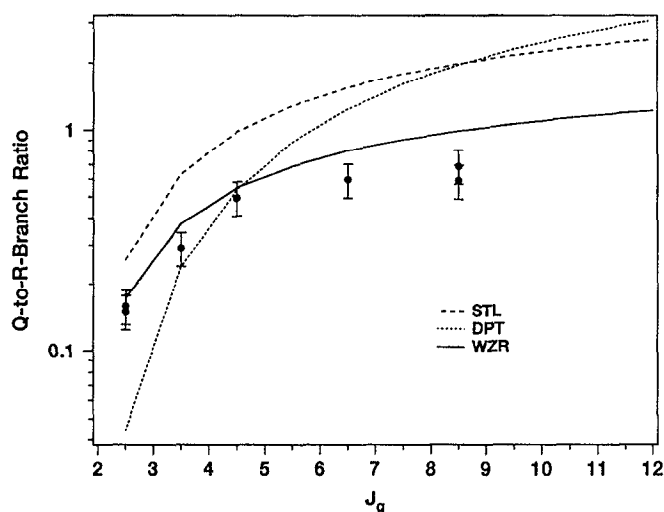

FIG. 8. Ratio of the integrated intensities for Q_1 and R_1 transitions that share a common initial state as a function of J_g. The dashed curve is the B_{ge}^2 saturated two-level model (STL) prediction for the Q-to-R-branch ratio, the dotted curve is the $B_{ge}^4 G_F^T(\epsilon_4,\epsilon_1,\epsilon_3,\epsilon_2;J_g,J_e)^2$ diagrammatic perturbation theory (DPT) prediction, and the solid curve is the $B_{ge}^2 G_F^T(\epsilon_4,\epsilon_1,\epsilon_3,\epsilon_2;J_g,J_e)^2$ empirical (WZR) prediction.

branch ratio. We have used a simple B_{ge}^2 dependence because the average degree of saturation of the data shown in Fig. 8 is $1.26I_{sat}^{ex}$ which corresponds to $B_{ge}^{1.96}$ according to the integrated MCECA model. The dotted curve in Fig. 8 is the $B_{ge}^4 G_F^T(\epsilon_4,\epsilon_1,\epsilon_3,\epsilon_2;J_g,J_e)^2$ diagrammatic perturbation theory (DPT) prediction where $G_F^T(\epsilon_4,\epsilon_1,\epsilon_3,\epsilon_2;J_g,J_e)$ is the total geometric factor of WZR1, Table II.[63] Recall that if $\Gamma_e = \Gamma_g$ these values apply to R-branch PC-DFWM signals. Inspection of Fig. 8 indicates that neither model is able to account for the fact that the Q-branch transitions are weaker than the R-branch transitions for high values of J_g even though the Q-branch absorption coefficients are larger (see Fig. 9).

The work of Farrow, Rakestraw, and Dreier[47] demonstrated that there is a reduced absorption coefficient dependence ($\sim B_{ge}^2$) at saturating laser intensities, and our polarization ratio data (Fig. 5) showed that the relative anisotropy of the total angular momentum distribution represented by the total geometric factors persists in the presence of saturating fields. Therefore, we have also plotted $B_{ge}^2 G_F^T(\epsilon_4,\epsilon_1,\epsilon_3,\epsilon_2;J_g,J_e)^2$ in Fig. 8 which is the solid curve (WZR). In Fig. 8 it is apparent that both a reduced absorption coefficient dependence and a total geometric correction are necessary to account for the observed Q-to-R-branch ratios. Note at $J_g = 4.5$ the DPT and WZR curves are equal, and both curves are in excellent agreement with the observed ratio. The agreement at $J_g = 4.5$ results from the fact the absorption coefficients for the $Q_1(4)$ and $R_1(4)$ transitions are equal, so the ratio is determined exclusively by the geometric correction. The agreement at other J_g values is not as good because the Q_1- and R_1-branch absorption coefficients are not equal, and therefore the transitions are not saturated to the same degree.

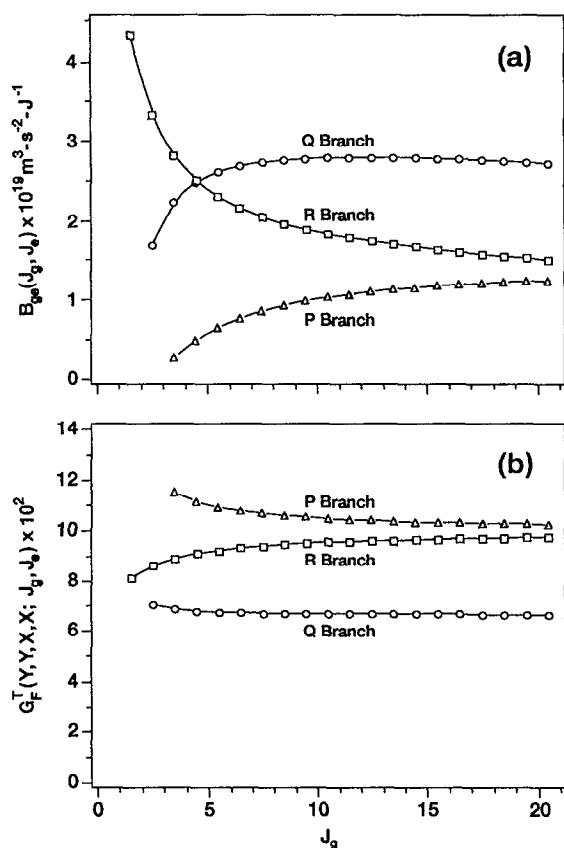Once more the simple introduction of the geometric fac-

FIG. 9. (a) The Einstein absorption coefficients as a function of J_g for the R_1-, Q_1-, and P_1-branch transitions of CH labeled -□-, -O-, and -△-, respectively. The absorption coefficients for the R_2-, Q_2-, and P_2-branch transitions are nearly the same because both the X and A states rapidly approach Hund's case (b) coupling as rotation increases. (b) Total geometric factors of WZR1, Table II for the $YYXX$ polarization configuration as a function of J_g with the same conventions as (a).

tors is able to explain the observed signal ratios with an accuracy in the range of 10%–30%. We noted in WZR1 that at saturating laser intensities higher order moments of the angular momentum distribution contribute to the DFWM signal; however, these data suggest that the first three moments are sufficient nevertheless to predict relative signal strengths at laser intensities up to approximately twice the saturation intensity.

E. Relative population distributions

In general DFWM signals must be corrected for differences in collision rates, absorption coefficients, and geometric factors before relative population distributions can be determined. Previous saturated DFWM temperature determinations employing broad-bandwidth excitation, however, have shown good agreement with thermocouple[6] and coherent anti-Stokes Raman scattering[8,11] measurements without applying collisional and geometric corrections; the only J-dependent corrections made in these determinations were for relative absorption coefficients ($I_{DFWM} \propto B_{ge}^2$). In these experiments the laser intensity was in excess of the saturation intensity, and the analysis only involved DFWM

signals from members of a single branch. We offer the following explanation for the apparent insensitivity of the DFWM signal to collisions and geometric corrections in these experiments and present the results of a rotational temperature analysis of the CH radical performed under similar conditions.

The reduced sensitivity to collisions is discussed first. The LFR calculations (Sec. I) for narrow-band DFWM of Doppler-broadened systems predict that the line-center DFWM signal is nearly independent of collisions at approximately $2I_{sat}^0$. This assertion is substantiated by their experimental data (Fig. 5 of Ref. 3 and Fig. 15 of Ref. 16) taken with a narrow-band excitation source. We can understand this result by considering the how collisions affect the DFWM signal for Doppler-broadened systems. Using the total collisional dependence of the Doppler-broadened reflectivity of Eq. (21), we find that the line-center DFWM signal of the AL model has a zero-order collisional rate dependence at approximately $0.5I_{sat}^0$. This value is in qualitative agreement with the LFR calculated value of $2I_{sat}^0$. Without employing the additional collisional dependence of Eq. (21) for Doppler-broadened systems, the line-center DFWM signal of the AL model is independent of collisions only when $I \gg I_{sat}^0$. This result is does not qualitatively agree with the LFR calculations.

By comparison we find using the total collisional dependence of the Doppler-broadened reflectivity of Eq. (22) that the line-center DFWM signal of the MCECA model has a zero-order collisional rate dependence at approximately $0.6I_{sat}^0$. The applicability of Eq. (22) to our experiments is validated by the fact that the Doppler-broadened correction is necessary to account for the magnitude of our experimentally measured reflectivities. Hence it is reasonable to assume that broad-bandwidth DFWM signals of Doppler-broadened systems exhibit a reduced collisional dependence at laser intensities approximately equal to $2I_{sat}^0$.

The independence of DFWM signals to geometric corrections results from that the fact that the total geometric factors are essentially constant for members of a single branch. As is shown in Fig. 9, the total geometric factors differ markedly for different branches, are J dependent for low J_g values, but are constant for each branch for values of J_g greater than three or four. We expect that once the geometric factors approach a high-J limit then the only remaining J-dependent corrections to saturated ($I \sim I_{sat}$) DFWM signal intensities for members of a single branch would arise from differences in absorption coefficients. We suggest that this behavior is the primary reason for the remarkable success of applying simple absorption coefficient corrections to determine relative population distributions from saturated DFWM signals.

We further emphasize this important point by presenting the results of a saturated DFWM rotational temperature analysis. In our rotational temperature determination we use Q-branch transitions recorded using the $YYXX$ PC-DFWM experimental configuration with the laser intensity maintained at approximately 1.7 times the experimental saturation intensity of the $Q_{1ef}(8)$ transition. The average degree of saturation of all the Q-branch transitions used in the analysis
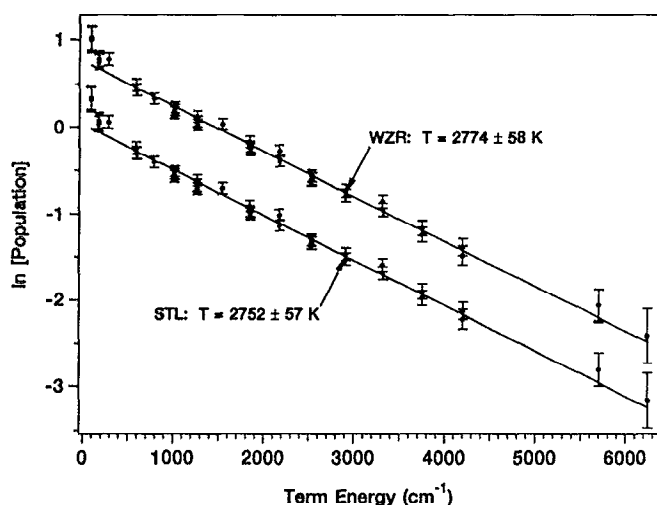
FIG. 10. Boltzmann plot of integrated Q-branch transitions for $2.5 \leqslant J_g \leqslant 20.5$ taken in the $YYXX$ polarization configuration. The power-broadened line widths of the transitions used in the analysis indicate that the average degree of saturation of these data is 1.6 I_{sat}^{ex}. The lower line (STL) represents a least-squares linear regression analysis using data corrected for the $B_{ge}^{1.85}$ dependence, and the upper line (WZR) represents data corrected for the $B_{ge}^{1.85} G_F^T(\epsilon_4,\epsilon_1,\epsilon_3,\epsilon_2;J_g,J_e)^2$ dependence. In both linear regression analyses data corresponding to $3.5 \leqslant J_g \leqslant 20.5$ of resolved Q_1 and Q_2 transitions are used and no collisional corrections are applied.

is 1.6I_{sat}^{ex} with a range of approximately 0.9 to 2.3I_{sat}^{ex} as determined from the power-broadened line widths. This average degree of saturation corresponds to a $B_{ge}^{1.85}$ dependence for the integrated DFWM signal intensities according to the MCECA model. A Boltzmann plot of integrated Q-branch transitions for $2.5 \leqslant J_g \leqslant 20.5$ is shown in Fig. 10. The lower line (STL) represents a least-squares linear regression analysis using data corrected for the $B_{ge}^{1.85}$ dependence, and the upper line (WZR) represents data corrected for the $B_{ge}^{1.85} G_F^T(\epsilon_4,\epsilon_1,\epsilon_3,\epsilon_2;J_g,J_e)^2$ dependence. In both linear regression analyses data corresponding to $3.5 \leqslant J_g \leqslant 20.5$ of resolved Q_1 and Q_2 transitions are used and no collisional corrections are applied.

We find that the geometric corrections only change the fitted temperature by 0.5%. This result is expected since the total geometric factors of the Q branch are nearly constant over the range $3.5 \leqslant J_g \leqslant 20.5$. The data at the smallest term energies ($J_g = 2.5-4.5$), however, deviate significantly from the data at larger term energies. Inspection of Fig. 9 shows that the Q branch the absorption coefficients are J dependent for low values of J_g. We showed for the Q-to-R-branch ratios in Sec. IV D that the applied corrections, i.e., $B_{ge}^2 G_F^T(\epsilon_4,\epsilon_1,\epsilon_3,\epsilon_2;J_g,J_e)^2$, are only accurate to 10%–30% when the relative absorption coefficients and geometric factors differ. Therefore using DFWM signal from members of a single branch and J_g values greater than three or four greatly reduces the error in determining the rotational temperature because both the absorption coefficients and total geometric factors are essentially J independent.

The degree of saturation of the data used in the analysis ranges from approximately 0.9I_{sat}^{ex} at $J_g = 3.5$ to 2.3I_{sat}^{ex} at $J_g = 20.5$. This range of saturation intensities corresponds to

approximately a 60% decrease in the population relaxation rate, Γ_0, from $J_g = 3.5$ to $J_g = 20.5$ using $I_{sat}^{ex} \propto b\Gamma_0/B_{ge}$. A decrease in the relaxation rate with increasing J_g is expected for CH in this flame because $\Gamma_0 \sim \Gamma_g \sim \Gamma_e \sim R$ and R generally decreases as the spacing between adjacent rotational levels increases.[64] Hence if the DFWM signal were sensitive to collisions, a 60% variation in the collisional rate would significantly affect the temperature obtained from the Boltzmann analysis. For example the temperature would increase by approximately 160 K (>5%) if the DFWM signal were inversely proportional to the collisional rate.

The temperature obtained from the linear regression analysis of the data corrected for the $B_{ge}^{1.85} G_F^T(\epsilon_4,\epsilon_1,\epsilon_3,\epsilon_2;J_g,J_e)^2$ dependence is 2774 ± 58 K. This value is in consistent (within 5%) with our previously reported[12] CH vibrational temperatures of 2642 ± 99 and 2882 ± 123 K obtained by LIF and DFWM, respectively. Because of the specific characteristics of the X and A states of CH, vibrational temperatures do not need to be corrected for relaxation, polarization, or saturation effects. This interesting aspect of high-pressure CH spectroscopy is discussed in detail in Ref. 12. Therefore the 5% agreement between the rotational temperature and vibrational temperatures suggests that the DFWM signal does in fact exhibit a reduced (less than linear) collisional dependence when $I \sim I_{sat}^{ex}$.

Finally, we comment on the rotational temperature error of 58 K (2%). This error is more indicative of the precision of these measurements rather than the accuracy because several significant assumptions were made in interpreting the observed DFWM signals using the MCECA model. Based on these assumptions and the results presented in this paper, a more realistic estimate of the accuracy of these measurements is 140 K (5%). This conclusion is also supported by the results of another ongoing project at Stanford which involves the investigation of trace radical species such as CH and C_2 in an atmospheric-pressure diamond synthesis reactor.[65–67] The reactor consists of an rf inductively coupled argon plasma seeded with hydrogen and methane. These studies have focused on measuring CH and C_2 concentration profiles and CH vibrational and rotational temperatures using saturated DFWM. The results of these measurements are consistent with the results of numerical simulations of the deposition environment over a temperature range of 2500–4000 K. Furthermore the agreement between the CH vibrational, rotational, and simulated temperatures has consistently been ~5%.[68–70]

V. CONCLUSIONS

We have experimentally evaluated the effects of polarization in DFWM spectroscopy from the weak- to the strong-field limit. The effects of polarization were rationalized using the ideas developed in WZR1 for the weak-field limit. The key results are that the saturation intensity is relatively independent of polarization and that the DFWM spatial effects represented by the weak-field geometric factors of WZR1 are applicable at laser intensities up to twice the saturation intensity. Furthermore we showed that polarization ratios measured with weak fields can be used to infer important relaxation information.

The error in applying the weak-field geometric factors to saturated DFWM signals was found to be in the range of 10%–30%. This degree of accuracy may be sufficient for determining energy transfer rates. In particular the sub-Doppler resolution offered by PC-DFWM would be advantageous for resolving energy transfer rate differences between different spin–orbit and Λ-doublet components that are difficult to resolve using LIF at these temperatures. In determining relative population distributions for temperature measurements, however, 10%–30% accuracy is often not sufficient.

We showed in Sec. IV that if the absorption coefficients and the total geometric factors of a set of transitions are nearly the same, relative population distributions accurate to 5% can be extracted from saturated DFWM signals. Such behavior is expected for members of a single branch once the absorption coefficients and the total geometric factors reach a high-J limit. Therefore, small values of J should be avoided in the analysis when accuracy is of primary importance. This result is an important finding because it substantiates a significant assumption in using two-level nondegenerate models to determine relative internal-state distributions of molecules. We also note that this finding is the same as that of Altkorn and Zare[57] for saturated LIF.

We supported this finding by presenting a rotational temperature analysis of the CH radical in an atmospheric-pressure flame. We employed a novel polarization configuration in this experiment which offered true zero-background detection and greatly discriminated against other intensity grating contributions to the DFWM signal. The laser intensity was maintained at approximately 1.7 times the experimental saturation intensity of the $Q_{1ef}(8)$ transition, and a PC-DFWM spectrum of the Q branch of the CH $A\,^2\Delta-X\,^2\Pi$ (0,0) band was obtained in the $YYXX$ polarization configuration. From a Boltzmann analysis a rotational temperature of 2774 ± 140 K was obtained. This rotational temperature is in good agreement with the average LIF and DFWM vibrational temperature of 2762 ± 160 K previously reported by our laboratory.

ACKNOWLEDGMENTS

[1] R. L. Abrams and R. C. Lind, Opt. Lett. **2**, 94 (1978); **3**, 205(E) (1978).
[2] R. L. Abrams, J. F. Lam, R. C. Lind, D. G. Steel, and P. F. Liao, in *Optical Phase Conjugation*, edited by R. A. Fisher (Academic, New York, 1983), Chap. 8, and references therein.
[3] R. L. Farrow and D. J. Rakestraw, Science **257**, 1894 (1992).
[4] G. Hall and B. J. Whitaker, J. Chem. Soc. Faraday Trans. **90**, 1 (1994).
[5] S. Williams, R. N. Zare, and L. A. Rahn, J. Chem. Phys. **101**, 1072 (1994).
[6] R. L. Farrow, D. J. Rakestraw, and T. Dreier, J. Opt. Soc. Am. B **9**, 1770 (1992).
[7] P. M. Danehy, E. J. Friedman-Hill, R. P. Lucht, and R. L. Farrow, Appl. Phys. B **57**, 243 (1993).
[8] T. Dreier and D. J. Rakestraw, Opt. Lett. **15**, 72 (1990).
[9] M. Winter and P. P. Radi, Opt. Lett. **17**, 320 (1992).
[10] B. Yip, P. M. Danehy, and R. K. Hanson, Opt. Lett. **17**, 751 (1992).
[11] T. Dreier and D. J. Rakestraw, Appl. Phys. B **50**, 479 (1990).
[12] S. Williams, D. S. Green, S. Sethuraman, and R. N. Zare, J. Am. Chem. Soc. **114**, 9122 (1992).
[13] D. R. Meacher, A. Charlton, P. Ewart, J. Cooper, and G. Alber, Phys. Rev. A **42**, 3018 (1990).
[14] J. Cooper, A. Charlton, D. R. Meacher, P. Ewart, and G. Alber, Phys. Rev. A **40**, 5705 (1989).
[15] G. Alber, J. Cooper, and P. Ewart, Phys. Rev. A **31**, 2344 (1985).
[16] R. P. Lucht, R. L. Farrow, and D. J. Rakestraw, J. Opt. Soc. Am. B **10**, 1508 (1993).
[17] D. Bloch and M. Ducloy, J. Opt. Soc. Am. **73**, 635 (1983); **73**, 1844(E) (1983).
[18] M. Ducloy, F. A. M. de Oliveira, and D. Bloch, Phys. Rev. A **32**, 1614 (1985).
[19] S. Le Boiteux, P. Simoneau, D. Bloch, F. A. M. de Oliveira, and M. Ducloy, IEEE J. Quantum Electron. QE-**22**, 1229 (1986).
[20] G. Grynberg, M. Pinard, and P. Verkerk, Opt. Commun. **50**, 261 (1984).
[21] M. Pinard, B. Kleinmann, and G. Grynberg, Opt. Commun. **51**, 281 (1984).
[22] G. Grynberg, M. Pinard, and P. Verkerk, J. Phys. (Paris) **47**, 617 (1986).
[23] P. Verkerk, M. Pinard, and G. Grynberg, Phys. Rev. A **35** (1987).
[24] G. P. Agrawal, Opt. Lett. **8**, 359 (1983).
[25] J. M. Khosrofian and B. A. Garetz, Appl. Opt. **22**, 3406 (1983).
[26] P. F. Bernath, C. R. Brazier, T. Olsen, R. Hailey, W. T. M. L. Fernando, C. Woods, and J. L. Hardwick, J. Molec. Spectrosc. **147**, 16 (1991).
[27] J. Hinze, G. C. Lie, and B. Liu, Astrophys. J. **196**, 621 (1975).
[28] N. L. Garland and D. R. Crosley, J. Quant. Spectrosc. Radiat. Transfer **33**, 591 (1985).
[29] J. Luque and D. R. Crosley, J. Quant. Spectrosc. Radiat. Transfer. (submitted).
[30] J. Brzozowski, P. Bunker, N. Elander, and P. Erman, Astrophys. J. **207**, 414 (1976).
[31] M. Danielson, P. Erman, A. Hishikawa, M. Larsson, E. Rachlew-Kallne, and G. Sundstrom, J. Chem. Phys. **98**, 9405 (1993).
[32] I. Kovács, *Rotational Structure in the Spectra of Diatomic Molecules* (American Elsevier, New York, 1969), Table 3.7, pp. 130.
[33] The Kovács line strengths for CH are tabulated in C. I. M. Beenakker, P. J. F. Verbeek, G. R. Mohlmann, and F. J. de Heer, J. Quant. Spectrosc. Radiat. Transfer **15**, 333 (1975).
[34] R. C. Hilborn, Am. J. Phys. **50**, 982 (1982), Eqs. (9) and (10).
[35] P. F. Bernath, J. Chem. Phys. **86**, 4838 (1987).
[36] R. J. Cattolica, D. Stepowski, D. Puecheberty, and M. Cottereau, J. Quant. Spectrosc. Radiat. Transfer **32**, 363 (1984).
[37] N. L. Garland and D. R. Crosley, Appl. Opt. **24**, 4229 (1985).
[38] N. L. Garland and D. R. Crosley, Chem. Phys. Lett. **134**, 189 (1987).
[39] R. G. Joklik and J. W. Daily, Combust. Flame **69**, 211 (1987).
[40] K. J. Rensberger, M. J. Dyer, and R. A. Copelend, Appl. Opt. **27**, 3679 (1988).
[41] D. E. Heard, J. B. Jeffries, and D. R. Crosley, Chem. Phys. Lett. **178**, 533 (1991).
[42] Y. Matsui, A. Yuuki, M. Sahara, and Y. Hirose, Jpn. J. Appl. Phys. **28**, 1718 (1989), Fig. 7.
[43] A. E. Siegman, *Lasers* (University Science Books, Mill Valley, 1986), pp. 663–667.
[44] T. S. Rose, W. L. Wilson, G. Wäckerle, and M. D. Fayer, J. Chem. Phys. **86**, 5370 (1987).
[45] M. Sargent III, M. O. Scully, and W. E. Lamb, Jr., *Laser Physics* (Addison-Wesley, Redwood City, 1974).
[46] In the case of moving absorbers, these spatial holes wash out to some extent because the absorbers may move through several wavelengths of the field in their lifetimes. However, the absorbers with near zero velocity will interact most strongly with the counterpropagating fields. As a result holes with a width related to Γ_{eg} are burned into the velocity distribution.
[47] Reference 6. These authors use the AL model whereas the MCECA model is used in our analysis. The line strength dependence on laser intensity is nearly the same, however, which can be seen by comparing Eqs. (8) and (13).
[48] M. S. Brown, L. A. Rahn, and T. Dreier, Opt. Lett. **17**, 76 (1992).
[49] R. Trebino, E. K. Gustafson, and A. E. Siegman, J. Opt. Soc. Am. B **3**, 1295 (1986).
[50] G. S. Agarwal, Phys. Rev. A **37**, 4741 (1988).

[51] The probe field (2) is delayed with respect to the forward pump field (1) by a distance (~6 cm) greater than six times the coherence length of the laser, and the backward pump field (3) is delayed with respect to the forward pump field by a distance (~16 cm) greater than eighteen times the coherence length. Furthermore the interaction length of the fields is limited by the flame diameter (0.1 cm) to a distance approximately one tenth the coherence length. Under these conditions we assume that the MCECA theory is applicable.

[52] The kinetics of four-level molecular systems has been discussed by many authors. Some references pertinent to our studies are R. P. Lucht and N. M. Laurendeau, Appl. Opt. **18**, 856 (1979). J. O. Berg and W. L. Shackleford, *ibid.* **18**, 2093 (1979). R. P. Lucht, D. W. Sweeney, and N. M. Laurendeau, *ibid.* **19**, 3295 (1980).

[53] The temporal response of the DFWM signal was found to be approximately Gaussian with a FWHM in the range of 13–15 ns using fast photomultiplier (Hamamatsu R2393P) and a 1 GHz digitizing oscilloscope (HP54510A) for all experimental conditions. This observation suggests that the signal pulse shape follows that of the incident laser pulses and that the system response is steady state.

[54] L. A. Rahn and M. S. Brown, Opt. Lett. (in press).

[55] S. Williams, L. A. Rahn, P. H. Paul, J. W. Forsman, and R. N. Zare, Opt. Lett. (submitted).

[56] S. Williams, R. N. Zare, and L. A. Rahn (in preparation).

[57] R. Altkorn and R. N. Zare, Annu. Rev. Phys. Chem. **35**, 265 (1984).

[58] B. W. Shore, *The Theory of Coherent Atomic Excitation* (Wiley, New York, 1990), Vol. I pp. 436–469 and Vol. II pp. 1343–1358.

[59] E. U. Condon and G. H. Shortley, *Theory of Atomic Spectra* (Cambridge University, Cambridge, 1935).

[60] R. N. Zare, *Angular Momentum* (Wiley, New York, 1988).

[61] D. G. Steel and J. F. Lam, Opt. Commun. **40**, 77 (1981).

[62] M. Ducloy and D. Bloch, Phys. Rev. A **30**, 3107 (1984), Eq. (46).

[63] For a nondegenerate two-level system, $|\mu_{ge}|^2 = |\mu_{eg}|^2$. For a degenerate two-level system, however, $(2J_g + 1)|\mu_{ge}|^2 = (2J_e + 1)|\mu_{eg}|^2$. The concentration difference, molecular line strength, and geometric factors of the DFWM intensity expression of WZR1 Eq. (2) have been normalized with respect to the ground level degeneracy $(2J_g + 1)$. See Eqs. (47)–(51) of WZR1. Therefore, in order to apply the geometric factors of WZR1, $|\mu_{ge}|^2 \propto B_{ge}$ must be used. Note that $|\mu_{ge}|^2$ has also been used in the two-level model expressions of Sec. III so that in the weak-field limit and for $N_g \gg N_e$ the two-level models will be equivalent to the WZR1 expressions derived rigorously.

[64] T. A. Brunner and D. Prichard, in *Dynamics of the Excited State*, edited by K. P. Lawley (Wiley, New York, 1982), pp. 589–641.

[65] T. G. Owano, C. H. Kruger, and M. A. Cappelli, Mater. Res. Soc. Symp. Proc. **190**, 131 (1991).

[66] M. A. Cappelli, T. G. Owano, and C. H. Kruger, J. Mater. Res. **5**, 2326 (1990).

[67] T. G. Owano, D. G. Goodwin, C. H. Kruger, and M. A. Cappelli, Proc. 2nd Int. Conf. on the New Diamond Science and Technology (Materials Research Society, Pittsburgh, 1991), p. 497.

[68] T. G. Owano, C. H. Kruger, D. S. Green, S. Williams, and R. N. Zare, Diamond Relat. Mater. **2**, 661 (1993).

[69] D. S. Green, T. G. Owano, S. Williams, D. G. Goodwin, R. N. Zare, and C. H. Kruger, Science **259**, 1726 (1993).

[70] T. G. Owano, E. H. Wahl, C. H. Kruger, D. S. Green, and R. N. Zare, Proc. of the 11th Int. Symp. on Plasma Chemistry, 416 (1993).